

VIP Very Important Paper

Special
Collection

Carbon Composite Anodes with Tunable Microstructures for Potassium-Ion Batteries

Shengming Zhang,^[a, b] Anastasia A. Teck,^[a] Zhenyu Guo,^{*[a]} Zhen Xu,^{*[a]} and Maria-Magdalena Titirici^{*[a]}

Among the post-lithium battery technologies, potassium-ion batteries are promising for cost-effective large-scale energy storage, as potash is an abundant resource. However, a major challenge is to understand the structure-performance relationships of carbon anodes for potassium-ion storage. In this study, we have designed a variety of carbon composite materials from 100% graphite to 100% soft carbon and in between, with tunable structural features to fundamentally understand the roles of different carbon structural features in potassium ion

insertion. We have found that the graphite-soft carbon composites (G-SC) show a high charge capacity of 280.2 mAh g^{-1} with an increased initial coulombic efficiency, representing the best reversibility among different carbon composites. Electrochemical impedance spectroscopy, cyclic voltammetry, and ex-situ structural characterizations have been applied to substantiate that the presence of soft carbon in G-SC inhibits the solid electrolyte interface layer formation and provides structural protection to the graphitic layers.

1. Introduction

Rechargeable batteries are required for a wide range of applications from portable electronic devices to electric vehicles and stationary electrical energy storage for the integration of intermittent renewable energy (e.g. wind, solar, etc.) into the grid.^[1] Lithium-ion batteries (LIBs) now dominate in energy storage devices due to the high energy density and reliable lifetime.^[2,3] However, sustainability is an issue for LIBs because lithium has an uneven global distribution and a low abundance of mere 0.0017 wt% in the earth's crust, resulting in rising prices and the risk of exhausting reserves.^[4] Other critical materials such as cobalt in the cathodes of LIBs are also suffering from rising prices,^[1] while expensive copper current collectors are used. Therefore, researchers are investigating alternative metal-ion batteries to reduce manufacturing costs and enhance sustainability.^[5] Elements of the same periodic group display similar physicochemical properties, indicating

that other alkali metals may be suitable replacements for lithium. The next two alkali metals are sodium and potassium, which are abundant, with 2.3 wt% and 1.5 wt%, respectively,^[6] in the earth's crust. Sodium-ion batteries (NIBs) were expected to provide similar performance to LIBs and have therefore received extensive attention. However, the design of carbon anodes has been problematic^[3] as sodium ions do not electrochemically intercalate into graphite at room temperature unless using expanded graphite and ether electrolytes, allowing the co-intercalation of solvated sodium ions into graphite.^[2] Hence, sodium ions can only be stored in active sites like defects and nanovoids in carbon materials when using carbonate electrolytes.

Differing from sodium ions, potassium-ion batteries (KIBs) can benefit from a similar graphite intercalation mechanism as LIBs^[3] and have achieved reversible capacities of over 200 mAh g^{-1} using graphite anodes. Moreover, KIBs are especially interesting for large scale energy storage which needs fast charge/discharge schemes. Because a small Stokes radius of potassium ions (3.6 \AA , vs 4.6 \AA of sodium ions and 4.8 \AA of lithium ions) helps reduce their (de-)solvation energies at electrode/electrolyte interface, fast kinetics and high ionic conductivity of potassium ions can be attained in carbonate solvents,^[2,7] promoting a high power density. Another advantage is the use of an inexpensive electrolyte system with a lower concentration (<0.8 M) of potassium ions. While research into suitable NIB anodes is on-going and most likely NIBs will soon become commercial, research into KIBs is equally promising.

It is documented that the electrochemical intercalation of potassium into graphite anodes mainly follows the three-stage progress on graphite intercalation compounds (GICs) formation including KC_{36} (stage 3), KC_{24} (stage 2) and KC_8 (stage 1) during the potassiation of graphite^[2,8] (Figure 1a). In Figure 1b, the galvanostatic charge/discharge (GCD) curves from our group show that a reversible specific capacity of graphite anodes can

[a] S. Zhang, A. A. Teck, Z. Guo, Z. Xu, Prof. M.-M. Titirici

Department of Chemical Engineering
Imperial College London
London SW7 2AZ, UK
E-mail: z.guo19@imperial.ac.uk
z.xu19@imperial.ac.uk
m.titirici@imperial.ac.uk

[b] S. Zhang

Department of Materials
University of Oxford
Oxford OX1 3PH, UK

 Supporting information for this article is available on the WWW under
<https://doi.org/10.1002/batt.202000306>

 An invited contribution to a joint Special Collection between
ChemElectroChem and Batteries & Supercaps dedicated to research Beyond
Lithium-Ion Batteries

 © 2020 The Authors. *Batteries & Supercaps* published by Wiley-VCH GmbH.
This is an open access article under the terms of the Creative Commons
Attribution License, which permits use, distribution and reproduction in any
medium, provided the original work is properly cited.

Table 1. The structural characterizations and their corresponding calculated data of graphite, G-SC 3:1 and SC.

	(002) Peak	I_b/I_G	Surface area [$m^2 g^{-1}$]	C 1s ^[a] [at%]	O 1s ^[a] [at%]
Graphite	26.6°	0.12	21.8	96.15	3.85
G-SC 3:1	26.5°	0.36	8.46	95.93	4.07
SC	25.4°	1.04	5.53	95.75	4.25

[a] at %: atomic percentage.

reach 282 mAh g⁻¹ in KIBs. The existence of defects and the carbon black additives in graphite anodes both increase the specific capacity of graphite anodes over their theoretical capacity (279 mAh g⁻¹). However, the potassiation of graphite anodes leads to a large volume expansion of over 60% due to the larger atomic radius of potassium (2.27 Å, vs 1.86 Å of sodium and 1.52 Å of lithium), thus decreasing the stability of graphite anodes.^[2] In addition, the first cycle of the potassiation of graphite anodes shows a low initial Coulombic efficiency of 54.08%. In comparison to graphite, soft carbon (SC) is a partially short-ranged, disordered and semi-graphitic carbon with relatively few defects and high crystallinity, which can be graphitized under high temperatures.^[9] Due to the disordered structures, more abundant functional groups and defects of SCs, various storage mechanisms including intercalation, adsorption, pore filling and defect adsorption allow the capacity of SCs to exceed that of graphite (Figure 1c).^[10] In this paper we combined the benefits of these two different carbon materials. Since research on KIBs is in its infancy, more efforts

should be paid into investigating the structure-performance relationships of carbon anodes.

To further improve KIB performance, researchers have investigated anode materials beyond graphite, such as soft carbon (SC),^[11] hard carbon (HC).^[11–13] Motivated by Jian et al.^[11] investigating HC-SC composite anodes for KIBs, herein we present, for the first time, G-SC composite anodes for KIBs to identify the optimized candidate and study the structure-performance relationships. Different ratios of G-SC composites (25 wt% G-SC 1:3, 50 wt% G-SC 1:1, 75 wt% G-SC 3:1, 90 wt% G-SC 9:1) using 0.8 M KPF₆ in ethylene carbonate and diethyl carbonate (EC-DEC) mixed solvents, ethylene carbonate and dimethyl carbonate (EC-DMC) mixed solvents, and diglyme solvents were systematically investigated by galvanostatic charge-discharge (GCD) to identify an optimal composition ratio and compare the electrochemical performance in different electrolytes. We have found that graphite-soft carbon composites (75 wt% G-SC 3:1) show an increased initial Coulombic efficiency of 67.3% with a high charge capacity of 280.2 mAh g⁻¹, which represents the best reversibility among different carbon composites. The G-SC composites also exhibit a higher working potential and a lower cost than composites than pure graphite. Following the optimization process, ex-situ characterization techniques including Raman spectroscopy, X-ray photoelectron spectroscopy (XPS) and X-ray diffraction (XRD) have been applied to elucidate that the presence of soft carbon in G-SC can inhibit solid electrolyte interface layer formation and provides structural protection to the graphitic layers.

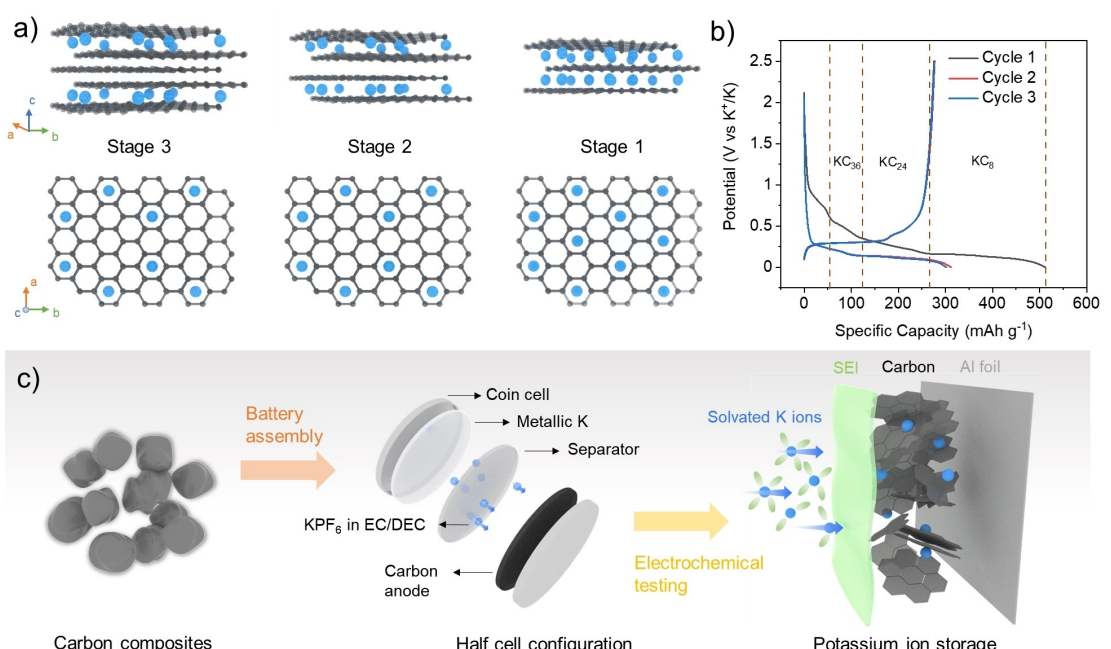


Figure 1. a) The illustration of three-stage intercalation mechanism in graphite anodes for potassium-ion batteries. b) The typical GCD curve of graphite anodes for potassium-ion batteries in a half-cell configuration from our group. c) Schematic illustration of the research performed in the project from material synthesis to battery fabrication and the mechanism study, which also exhibit the various storage mechanisms including intercalation, adsorption, pore filling and defect adsorption of carbon composites.

Experimental Section

Material Synthesis

Graphite powder (<20 µm, synthetic) was purchased from Sigma-Aldrich and used as received. Soft carbon (SC) was prepared via pyrolysis of mesophase pitch as precursors (MP, Bonding Chemical, USA) in a tube furnace at 1100°C for 2 hrs under N₂ atmosphere. All G-SC composites were synthesized by mixing graphite with pitch precursor in the desired mass fractions before the annealing process in a tube furnace at 1100°C for 2 hrs under N₂ flow with a heating rate of 5°C min⁻¹.

Electrochemical Characterization

The working electrodes (anodes) were prepared by mixing and milling 80 wt% of the selected sample with 10 wt% of carbon black (Alfa-Aesar) to improve conductivity and 10 wt% of poly-vinylidene difluoride (PVDF, from Sigma-Aldrich) as a binder in N-Methyl-2-pyrrolidone (NMP, from Sigma-Aldrich). The homogeneous slurry was pasted onto an Al foil (MTI Corporation) for the first-stage mild drying at 50°C for 2 hrs, ensuring the even deposition of a dense active material layer. The dried anodes were cut into square pieces (area of 0.64 cm⁻²) with an active material loading of 2–2.5 mg cm⁻², while the mass of individual anode was measured and recorded. The pre-dried anodes were further desiccated at 105°C under vacuum overnight and then transferred into an argon-filled glovebox (mBraun, H₂O, O₂<0.5 ppm). In the half cell configuration, potassium metal foil with a diameter of 10 mm was used as the counter and a reference electrode at the same time, and glass fiber (Whatman, GF/D Glass microfiber filters) with a diameter of 16 mm was served as a separator. The three electrolytes used (EC-DEC in 1:1 v%, EC-DMC in 1:1 v% and diglyme) have the same salt concentration of 0.8 M KPF₆. The stainless-steel CR2032 coin cells (MTI Corporation) were compacted using a gas-driven crimping (MTI Corporation) at a gauge pressure of 120 Psi. All the electrochemical measurements were conducted at room temperature and pressure. Galvanostatic charge-discharge (GCD) profiles at a voltage window of 0–2.5 V (vs. K⁺/K) were recorded on a LAND CT 2001 A battery testing system at different current densities. Cyclic voltammetry (CV) at 0.1 mV s⁻¹ and electrochemical impedance spectroscopy (EIS) from 100 kHz to 0.01 Hz were measured on an Autolab PGSTAT204 electrochemical workstation.

Structural Characterization

The active materials were dried at 105°C in a vacuum oven overnight before performing structural characterization. For ex-situ characterization, coin cells were unpacked using a crimper within a disassembling module after the first cycle of discharging and charging with further discharging at a current density of 0.1 C (27.9 mA g⁻¹). The anode was removed from the stainless-steel spacer, washed with the corresponding electrolyte without the salt and dried at 105°C in a vacuum oven overnight. X-ray photoelectron spectroscopy (XPS) was conducted using a Thermo Fisher K-Alpha⁺ XPS facility, and data were fitted using the Avantage software. Raman spectroscopy was performed on a Thermo Scientific DXR3 instrument and results were fitted using the Lorentzian method. The morphology of samples was obtained from Scanning electron microscopy (SEM), using an LEO Gemini 1252 FEG-SEM machine. X-ray diffraction (XRD) was performed in an X'Pert PRO PANalytical using 40 mA and 40 kV power settings. The Brunauer-Emmett-Teller (BET) method and density-functional-theory (DFT) method were used to evaluate the surface area and pore size distribution from the N₂ adsorption/desorption isotherm by a Micromeritics 3 Flex Physisorption instrument.

2. Results and Discussion

To gain information about the electrochemical behavior and performance of G-SC composites in different electrolytes (EC-DEC, EC-DMC and diglyme), the 2nd cycle capacity and the initial Coulombic efficiencies were summarized in Figure 2 with their corresponding GCD curves in Supporting Information (Figure S1-S4). As for the initial Coulombic efficiencies in Figure 2a, graphite, SC and G-SC composites in EC-DEC and EC-DMC have similar trends where G-SC 3:1 has the highest Coulombic efficiencies compared with the pristine graphite and SC. It is worth mentioning that G-SC 3:1 always exhibits the best initial Coulombic efficiency among three testes electrolytes. In the case of diglyme, all graphite-contained composites exhibit low capacities around ~180 mAh g⁻¹ in diglyme because of the co-intercalation of solvated potassium ions into graphitic layers. As for the reversible capacities in Figure 2b, the EC-DEC is the most promising electrolyte with generally higher

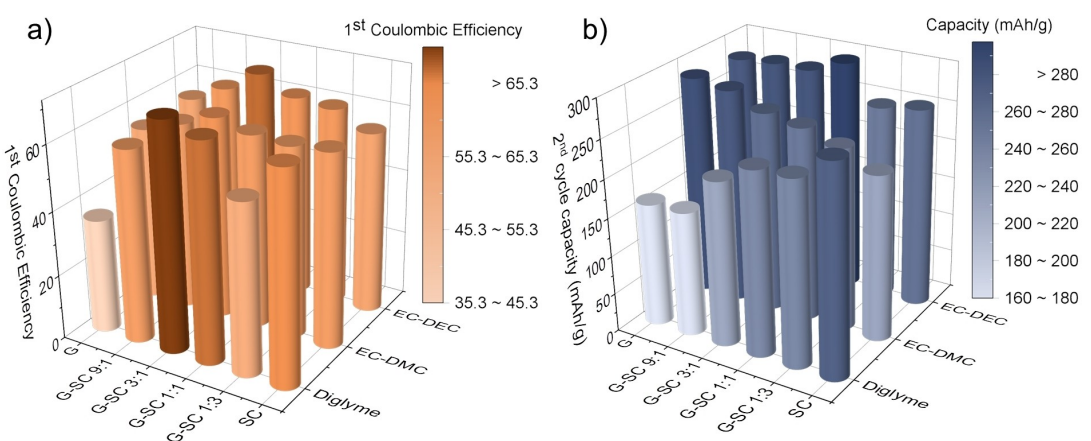


Figure 2. a) The initial Coulombic efficiencies of different anode materials in three electrolytes. b) The 2nd cycle reversible capacities of different anode materials in three kinds of electrolytes.

reversible capacities for all G-SC composites compared to EC-DMC and diglyme. Remarkably, in EC-DEC, the G-SC 3:1 exhibits the initial Coulombic efficiency of 67.3% and a promising reversible capacity of 280.2 mAhg^{-1} , which are further discussed in the following parts to investigate its structure-performance correlation.

2.1. Structural Characterization

Scanning electron microscopy (SEM) discloses the morphologies of pure graphite (G), G-SC 3:1 and pure SC (Figure 3a). SEM images of G-SC composites show that after the pyrolysis of the graphite powder together with the MP, the molten MP covers the graphite powder and creates a continuous structure. Qi et al.^[14] demonstrated that during the pyrolysis process, the molten pitch can not only act as a cross-linking agent between the different graphitic crystallites but also fill the existing open pores in graphite. Based on N_2 adsorption/desorption isotherms (Figure 3e), the calculated BET surface area of pure graphite dramatically decreases from $21.8 \text{ m}^2 \text{ g}^{-1}$ to $8.46 \text{ m}^2 \text{ g}^{-1}$ by adding 25 wt% of SC into the graphite. Small-angle X-ray scattering and BET surface area results together indicate some open pores were blocked by the MP coating, and these blocked open pores are inaccessible to the electrolyte, reducing the possibility of the loss of electrolyte consumption forming solid electrolyte interface (SEI) on the surface of open pores.^[15,16] Based on our

previous studies on SC pore filling process^[15] and thermogravimetric analysis (TGA) data of mesophase pitch from reported literature,^[14] mesophase pitch will form liquid phase at a very low temperature (300°C) and then infuse into the pore structures of graphite powders, followed by the chemical combination between the graphite and soft carbon (from 500°C). However, the intrinsic pore structures of carbon materials are quite stable at around 300°C if there is no activation agent, and only the temperatures around 1300°C can obviously shrink the intrinsic pore structures.^[17] Therefore, the pore filling happens before the temperature rises to 1100°C , and 1100°C is not high enough to make the intrinsic pore structures of graphite shrink. The surface morphology and cross-sectional area for prepared anodes are also shown in Figure S5, where the thickness of aluminum foil and the layer of active material are $18 \mu\text{m}$ and around $50 \mu\text{m}$, respectively. The thickness and active material loading were similar for all prepared anodes. From Raman Spectra in Figure 3b, the Lorentzian method is used to fit the D peak ($\sim 1350 \text{ cm}^{-1}$) and G peak ($\sim 1580 \text{ cm}^{-1}$), and the intensity ratio of D peak to G peak (I_D/I_G) is used to determine the defects and disordered structures of synthesized materials. I_D/I_G for pure graphite powder, pure G-SC powder and pure SC powder are 0.12, 0.36 and 1.04, respectively. According to the three-stage model for graphite and amorphous carbon proposed by A. C. Ferrari,^[18-20] pure graphite, SC and their composites are all classified in Stage 1, representing the transition from graphite to the

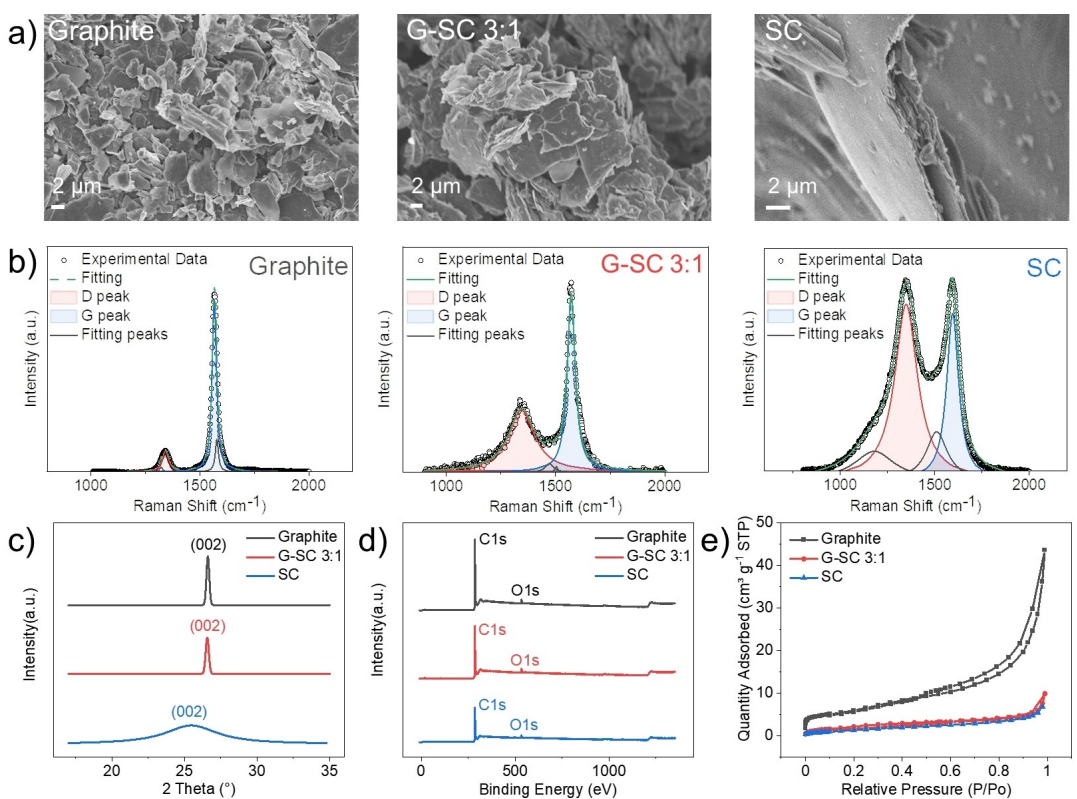


Figure 3. a) SEM images of graphite (left), G-SC 3:1 (middle) and SC (right). b) Fitted Raman spectra for graphite (left), G-SC 3:1 (middle) and SC (right). c) The XRD patterns of graphite, G-SC 3:1 and SC. d) The XPS spectra of graphite, G-SC 3:1 and SC. e) The N_2 adsorption/desorption isotherms (77 K) of graphite, G-SC 3:1 and SC.

nanocrystalline graphite. The I_D/I_G ratios increase from pure G, G-SC 9:1, G-SC 3:1, G-SC 1:1, G-SC 1:3 to pure SC as listed in Table S1, indicating an increased defective structure with additional SC, which correlates to Stage 1 behavior. This trend is also confirmed by the (002) peaks of XRD patterns labeled in Figure 3c. The SC (002) peak is located at 25.4° with a larger interlayer spacing of 3.48 \AA , indicating that SC has a more amorphous structure than that graphite. Although G-SC 3:1 contains 25 wt% SC, the interlayer spacing and (002) peak of G-SC 3:1 is nearly the same as that of graphite. From the C1s and O1s signals in the XPS, the pristine SC synthesized from MP has a higher oxygen content (4.25 at%) than graphite powder (3.85 at%), and the oxygen content of the G-SC 3:1 (4.07 at%) is in between the two, which means adding SC can introduce more oxygen heteroatoms into the carbon structures.

For the choice of annealing temperatures, 1100°C is a suitable temperature to make sure the SC has enough conductivity to facilitate the ion diffusion when employed as the electrodes. Second, 1100°C would not make the intrinsic pore structures of other carbon materials including graphite and hard carbon shrink, which can prove the function of SC pore filling as mentioned before. In addition, 1100°C is a relative low annealing temperature compared with other reported literature on carbon anodes,^[21] thus decreasing the energy consumption in terms of sustainability and maintaining

the optimized electrochemical performance of carbon anodes at the same time.

2.2. Electrochemical Characterization

The electrochemical characterizations of graphite, G-SC 3:1 and SC in EC-DEC are illustrated in Figure 4. GCD tests were performed to investigate the typical curves of charging and discharging, showing the plateau/sloping region, the initial irreversible capacity loss and working potential for each sample (Figure 4a). During the first cycle of potassiation, the initial Coulombic efficiencies of graphite, G-SC 3:1 and SC are 54.1%, 67.3% and 57.8% respectively. The irreversible capacity during the first cycle results from irreversible potassium ion insertion and solid electrolyte interface (SEI) formation due to electrochemical reactions between electrolyte and electrode.^[15,16] From the GCD curves in the first cycle (Figure 4a), the irreversible capacity is mainly derived from 1.0 V to 0.1 V (vs. K^+/K), which is in agreement with the first cycle of CV curves (Figure 4b). In Figure 4b, CV curves confirm SEI layer formation and irreversible K-ion intercalation during the first cycle by the disappearance of SEI cathodic peaks from 1.0 V to 0.1 V (vs. K^+/K) between the first cycle and following cycles.

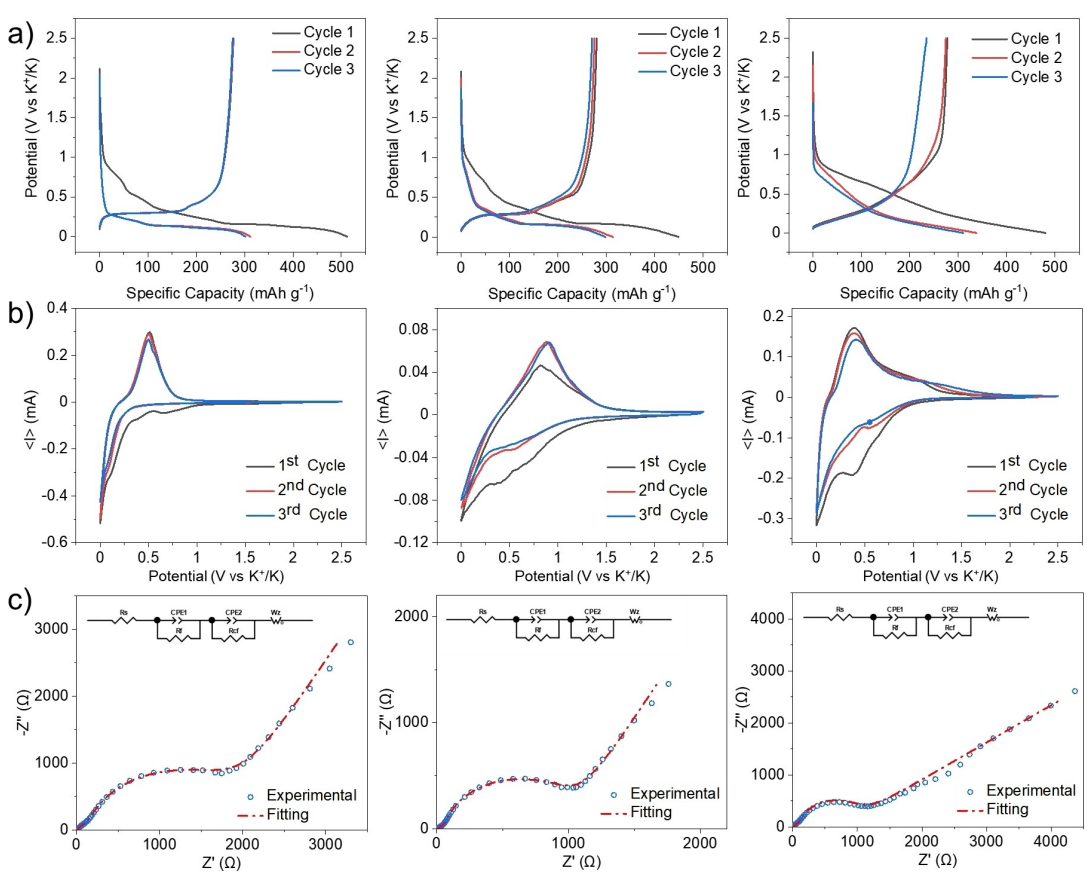


Figure 4. a) GCD curves at 0.1 C of G (left), G-SC 3:1 (middle) and SC (right). b) CV curves of G (left), G-SC 3:1 (middle) and SC (right). c) EIS curves of G (left), G-SC 3:1 (middle) and SC (right).

The diffusion-controlled intercalation of potassium ions in graphite shows a semi-plateau GCD curve from 0.5 V to 0.01 V (vs. K⁺/K) via GICs staging storage mechanism, while the surface-controlled adsorption of potassium ion on defects dominates in SC and cause a sloping GCD curve from 1.0 V to 0.01 V (vs. K⁺/K), according to the structural characterizations in Figure 3b and c. In Figure 4a, the GCD curve for G-SC 3:1 is characteristic of both intercalation and adsorption mechanism, and the working potential (depotassiation & anodic current) of G-SC 3:1 at ~0.8 V is higher than those of both graphite and SC at 0.5 V and 0.4 V (vs. K⁺/K), respectively. Additionally, the CV peak at 0.8 V demonstrates that the working potential of G-SC 3:1 is broader than pure graphite and SC. Correlating with XRD, Raman and XPS spectra (Figure 3b and c), G-SC 3:1 has defects and more active sites for surface-controlled adsorption (e.g. defects and functional groups) and diffusion-controlled insertion (e.g. intercalation and nano-pore filling), leading to a broad (de-)potassiation potential. For all composites, both the potentials of the plateaus and slope regions are above the plating potential of potassium metal (below 0 V vs K⁺/K), thus reducing the hazards of dendrite growth.

EIS was conducted to disclose the interface conditions and resistances at the anode by fitting a typical Nyquist plot for the electrodes after cycling at their respective ending open-circuit voltage (OCV). The equivalent circuits are displayed in Figure 4c, and the Nyquist plots are fitted according to the Randles circuits [Eq. (1)].^[22]

$$Z = R_s + \frac{1}{j\omega C_1 + \frac{1}{R_f}} + \frac{1}{j\omega C_2 + \frac{1}{R_f}} + W_z \quad (1)$$

where R_s (Ω) is the resistance in the electrolyte, R_{ct} (Ω) is the charge-transfer resistance, R_f (Ω) is the resistance of the SEI film. C_1 and C_2 represent the double-layer capacitance for two interfaces respectively, and W_z is the Warburg element of the circuit. Two consecutive semicircles emerge in the high-frequency regions (~13k Hz) and moderate frequency region (~100 Hz) corresponding to SEI layer formation and intrinsic charge transfer through the electrode interface, respectively, following the linear region at low frequency (~0.1 Hz) representing the Warburg diffusion of potassium ions from the electrolytes to the bulk carbon.^[23,24] Detailed resistance data and equivalent circuit fitting are in Figure S8. The largest charge transfer resistance (1600 Ω) and resistance of SEI layer (104.9 Ω) have been found for graphite, compared to that of G-SC 3:1 (917 Ω and 43.7 Ω) and SC (718 Ω and 18.5 Ω) and, depicting that the pristine graphite has sluggish charge transfer kinetics and intensive SEI layer formation. The intercalation mechanism of graphite is a diffusion-controlled reaction, causing the large charge transfer resistance. Surprisingly, the SC has the lowest SEI film resistance and fastest charge transport across the electrolyte interface. The amorphous and open layer structure with a larger interlayer spacing of SC can shorten ion pathways to speed up reaction based on adsorption mechanism. By combining SC with graphite, the charge transfer resistance changes from 1600 Ω to 917 Ω in G-SC 3:1 as proof of faster electrochemical kinetic at the interface

between liquid EC-DEC electrolyte and G-SC 3:1 electrode. Additionally, the lower SEI film resistance of G-SC 3:1 does verify its mild SEI layer formation compared to graphite and explains the reason for its improved initial Coulombic efficiency.

2.3. Ex-Situ Mechanism Study

The structural changes in the anode materials before and after potassium storage were investigated using ex-situ XRD and Raman as shown in Figure 5. The ex-situ samples were measured after the potassiation of the second cycle. For both cycled graphite and G-SC 3:1 in Figure 5a, pairs of small peaks are located at 19.8° & 32.6°, and 22.8° & 29.7° which correspond to GICs of KC_{24} and KC_{36} , respectively. It is obvious that the G-SC 3:1 composite still exhibits an intercalation mechanism with GICs peaks. As for the SC, the absence of representative sharp peaks reflects the potassium storage is dominated by adsorption rather than intercalation. The pristine graphite and G-SC 3:1 electrode both show the characteristic sharp intrinsic graphite peak at a 2-theta angle of 26.6° and 26.5° respectively. For the cycled graphite sample, the characteristic peaks shift positively to 27.4° with a broadened full width at half maximum (FWHM) after full potassiation. According to Bragg's Law, the average spacing between the graphitic layer decreases from the intrinsic 3.33 Å to compressed 3.24 Å. This phenomenon leads us to hypothesize that the unfavorable intercalation of potassium-ions into graphite expands one edge of graphite layer structure and tilts the other side of the graphite layer resulting in compressed smaller spacing, leading to a reduced reversible capacity and stability of graphite materials. Figure 6a illustrates the schematic diagram of unfavorable intercalation with accumulated potassium ions at one side, thus narrowing graphite layers at the other side.^[6] The unfavorable intercalation is also related to the charge and discharge rates used. If potassium intercalation rate is faster than the diffusion rate of potassium towards the other end of the graphite layer, unfavorable intercalation on account of potassium accumulation at one end of graphite occurs.^[25] Compared with graphite, a smaller positive shift can be observed in the cycled G-SC 3:1. By adding SC, the expanded graphitic layer spaces of G-SC 3:1 can facilitate the ion diffusion while decreasing the unfavorable intercalation. It is worth mentioning that, after full potassiation at 0.1 C, the GICs like KC_8 are not completely formed, which prevents the graphite anode from reaching its full theoretical capacity. These GICs also contain 'dead' potassium remaining in the structure. As illustrated in Figure 6b, the 'dead' potassium can result in local bending of the graphite layer which confines itself, while the accumulation of 'dead' potassium further reduces the lifetime and distorts the graphitic structure. The first cycle of potassium storage causes the (002) peak of SC to shift to a smaller angle. However, the shift and bending of the (002) peak are effectively inhibited in G-SC 3:1 after full potassiation, which demonstrates that SC also has a protective role to maintain the physical structure of graphite layers and avoid the distortion of graphite layers. Therefore, this protec-

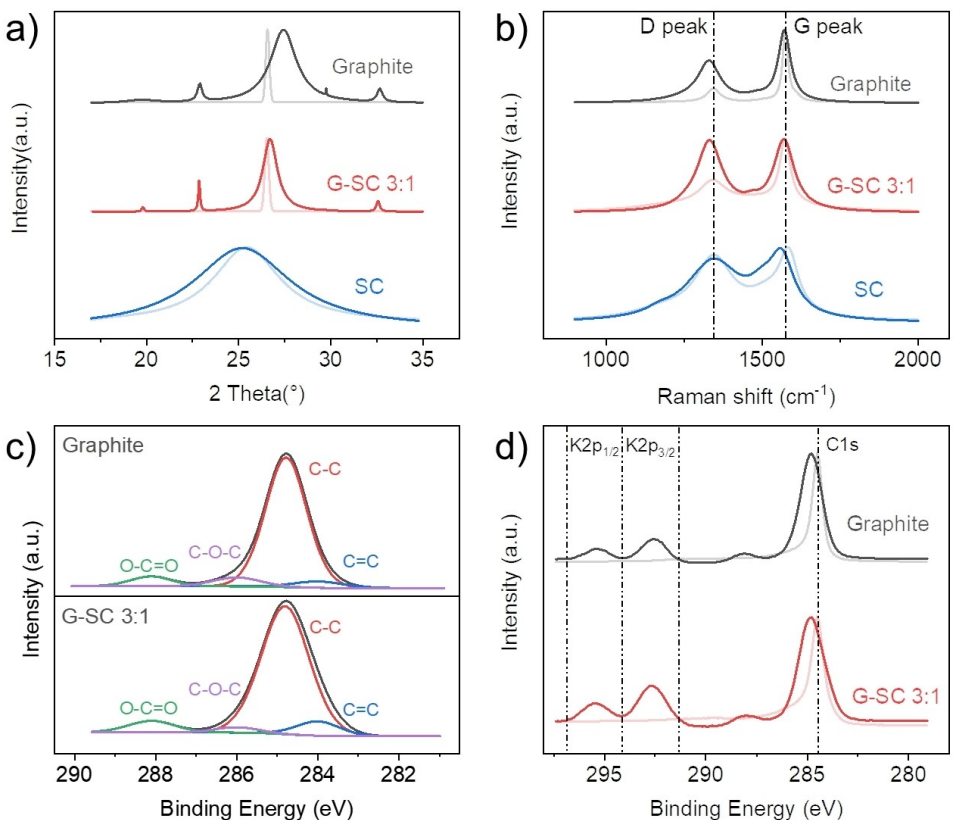


Figure 5. a) Ex-situ XRD patterns of G, G-SC 3:1 and SC (lighter colors represent pristine samples, and darker colors represent cycled samples). b) Ex-situ Raman spectra of G, G-SC 3:1 and SC (lighter colors represent pristine samples, and darker colors represent cycled samples). c) Fitted XPS O1s scan of pristine G and G-SC 3:1. d) Ex-situ XPS O 1s scan of G and G-SC 3:1 (lighter colors represent pristine samples, and darker colors represent cycled samples).

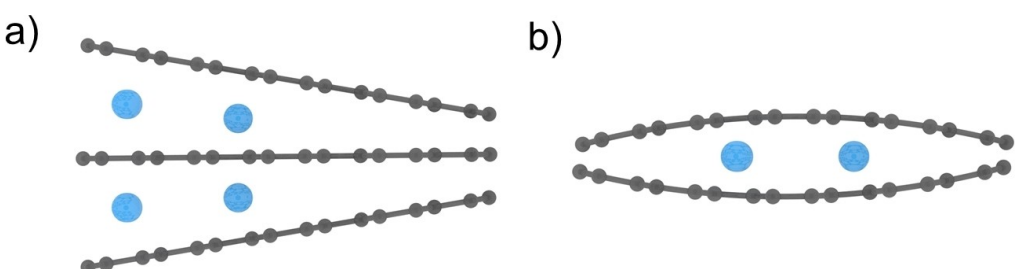


Figure 6. a) Unfavorable intercalation with accumulated potassium-ions at one edge of graphite and b) local bending of the graphite layer locking potassium-ions.

tion can enhance the structural integrity of the G-SC 3:1 by improving elasticity.

The details of the Raman spectra fitting in for I_D/I_G can be found in Figure S12, Supporting information. The I_D/I_G intensity ratio is 0.187, 0.403 and 1.07 for pristine graphite, G-SC 3:1 and SC electrodes (with PVDF and carbon black). After potassiation, the I_D/I_G intensity ratio increases to 0.546, 1.00 and 1.01 for cycled graphite, G-SC 3:1 and SC, respectively (Figure 5b). Pristine graphite, pristine G-SC 3:1 and pristine SC are all located in Stage 1 of the three-stage model proposed by A. C. Ferrari.^[18–20] After potassiation, the position of G peaks ($\sim 1580\text{ cm}^{-1}$) for graphite and G-SC 3:1 remains nearly unchanged without splitting of G peaks, proving cycled graphite

and cycled G-SC remain in Stage 1, while the I_D/I_G ratios of both G and G-SC 3:1 increase, inferring the transition from a graphitic to a nanocrystalline graphitic structure by the insertion of potassium ions. The percentage increase of I_D/I_G for G-SC 3:1 (148%) is smaller than that for graphite (192%) due to less structural change in G-SC 3:1, which further confirms the effective protection offered by the introduction of SC to the graphitic structure. In contrast, the soft carbon G peak shifts from 1580 cm^{-1} to 1561 cm^{-1} with an apparent broadening of the D peak after potassiation, meaning that cycled SC enters Stage 2. As the G peak shifts to $\sim 1561\text{ cm}^{-1}$ and I_D/I_G of the SC decreases from 1.07 to 1.01, its structure starts to change from nanocrystalline graphite to amorphous carbon, but the struc-

ture of SC is still more stable compared with graphite. Overall, the ex-situ XRD and Raman results have shown that the introduction of SC is beneficial to the structural stability, and G-SC 3:1 shows the smallest structural change, thus showing the best performance with the highest initial Coulombic efficiency (ICE).

Except for evaluating the deformation of graphite layers, XPS was conducted to investigate the SEI layer species on the anode surface after potassiation. Two peaks of C1s and O1s in pristine materials and four peaks of C1s, K2p, K2s and O1s in cycled samples were observed in XPS full scan (Figure 5c, 5d and Figure S10). In Figure 5c, the fitted C1s scans of pristine graphite and G-SC 3:1 show the existence of C—O—C and C=O=C bonds. In Figure 5d, the two minor peaks around 280 eV from cycled samples are K2p_{1/2} and K2p_{3/2} which proves the formation of SEI contains irreversible reactions of potassium decomposition of electrolytes on the surface of anodes. Furthermore, the binding energy of C1s peaks in cycled graphite and G-SC 3:1 both positively shift, which means the C—O—C and C=O=C bonds increase because of the SEI formation after potassiation. However, the oxygen level of pristine graphite is 3.85 at% which increases to 15.62 at% after the potassiation, while the oxygen level of pristine G-SC 3:1 significantly increases from 4.05 at% to 20.18 at% after the potassiation (Figure S10, Supporting information). Correlating the EIS of G-SC 3:1, the higher oxygen components of SEI in cycled G-SC 3:1 can enhance the wettability of electrodes and improve the interfaces of electrode/SEI/electrolyte, leading to faster charge transfer kinetics.^[26] Overall, the ex-situ XPS analysis is inconsistent with the synergic effect of graphite and SC for the better electrochemical performance of G-SC 3:1.

3. Conclusions

We presented a detailed study of G-SC composites proving the synergic effect between graphite and soft carbon, contributing to the excellent performance of G-SC 3:1 including the optimized ICE of 67.3% and reversible capacities of 280.2 mAh g⁻¹, when compared with pure graphite and SC. The introduction of soft carbon into G-SC 3:1 can tune the defects and other active sites for surface-controlled adsorption (e.g. defects and functional groups) and diffusion-controlled insertion (e.g. intercalation and nano-pore filling) with a broad working potential, which allows the faster kinetics of ion diffusion and more active sites for ion storage in the carbon structures. The higher oxygen components in SEI of cycle G-SC 3:1 can improve the interfaces of electrode/SEI/electrolyte, leading to faster charge transfer kinetics as well. Also, the addition of soft carbon provides structural protection to the graphitic layers, which can result in minor structural changes.

Acknowledgments

All authors are grateful for the grants from Engineering and Physical Sciences Research Council (EP/R021554/2, EP/S018204/2)

as well as Science and Technology Facilities Council (STFC) Batteries Network (ST/R006873/1). Z.X. and Z.G. acknowledge and China Scholarship Council for the funding support. S. Z. and A. T. appreciate the award of Henri Sawistowski Fellowship.

Conflict of Interest

The authors declare no conflict of interest.

Keywords: potassium-ion batteries • carbon composite anodes • graphite • soft carbon • synergistic effect

- [1] B. Dunn, H. Kamath, J. M. Tarascon, *Science* **2011**, *334*, 928–935.
- [2] Y. Li, Y. Lu, P. Adelhelm, M. M. Titirici, Y. S. Hu, *Chem. Soc. Rev.* **2019**, *48*, 4655–4687.
- [3] J. C. Pramudita, D. Sehrawat, D. Goonetilleke, N. Sharma, *Adv. Energy Mater.* **2017**, *7*, 1602911.
- [4] J.-M. Tarascon, *Nat. Chem.* **2010**, *2*, 510–510.
- [5] S. P. Kuksenko, *Russ. J. Electrochem.* **2013**, *49*, 67–75.
- [6] Z. Jian, W. Luo, X. Ji, *J. Am. Chem. Soc.* **2015**, *137*, 11566–11569.
- [7] Y. Matsuda, H. Nakashima, M. Morita, Y. Takasu, *J. Electrochem. Soc.* **1981**, *128*, 2552–2556.
- [8] L. Fan, R. Ma, Q. Zhang, X. Jia, B. Lu, *Angew. Chem. Int. Ed.* **2019**, *58*, 10500–10505.
- [9] B. Cao, H. Liu, B. Xu, Y. Lei, X. Chen, H. Song, *J. Mater. Chem. A* **2016**, *4*, 6472–6478.
- [10] M. Winter, J. O. Besenhard, M. E. Spahr, P. Novák, *Adv. Mater.* **1998**, *10*, 725–763.
- [11] Z. L. Jian, S. Hwang, Z. F. Li, A. S. Hernandez, X. F. Wang, Z. Y. Xing, D. Su, X. L. Ji, *Adv. Funct. Mater.* **2017**, *27*, 1700324.
- [12] Z. Jian, Z. Xing, C. Bommier, Z. Li, X. Ji, *Adv. Energy Mater.* **2016**, *6*, 1501874.
- [13] C. Vaalma, G. A. Giffin, D. Buchholz, S. Passerini, *J. Electrochem. Soc.* **2016**, *163*, A1295-A1299.
- [14] Y. Qi, Y. Lu, F. Ding, Q. Zhang, H. Li, X. Huang, L. Chen, Y. S. Hu, *Angew. Chem. Int. Ed.* **2019**, *58*, 4361–4365.
- [15] F. Xie, Z. Xu, A. C. S. Jensen, H. Au, Y. Lu, V. Araullo-Peters, A. J. Drew, Y. S. Hu, M. M. Titirici, *Adv. Funct. Mater.* **2019**, *29*, 1901072.
- [16] Z. Xu, F. Xie, J. Wang, H. Au, M. Tebyetekerwa, Z. Guo, S. Yang, Y. S. Hu, M. M. Titirici, *Adv. Funct. Mater.* **2019**, *29*, 1903895.
- [17] Y. M. Li, Y. S. Hu, M. M. Titirici, L. Q. Chen, X. J. Huang, *Adv. Energy Mater.* **2016**, *6*, 1600659.
- [18] A. C. Ferrari, D. M. Basko, *Nat. Nanotechnol.* **2013**, *8*, 235–246.
- [19] A. C. Ferrari, J. C. Meyer, V. Scardaci, C. Casiraghi, M. Lazzeri, F. Mauri, S. Pisacane, D. Jiang, K. S. Novoselov, S. Roth, A. K. Geim, *Phys. Rev. Lett.* **2006**, *97*, 187401.
- [20] A. C. Ferrari, J. Robertson, *Phys. Rev. B* **2000**, *61*, 14095–14107.
- [21] C. Zhao, Q. Wang, Y. Lu, B. Li, L. Chen, Y.-S. Hu, *Sci. Bull.* **2018**, *63*, 1125–1129.
- [22] Y. Shao, M. F. El-Kady, J. Sun, Y. Li, Q. Zhang, M. Zhu, H. Wang, B. Dunn, R. B. Kaner, *Chem. Rev.* **2018**, *118*, 9233–9280.
- [23] L. Xiao, Y. Cao, W. A. Henderson, M. L. Sushko, Y. Shao, J. Xiao, W. Wang, M. H. Engelhard, Z. Nie, J. Liu, *Nano Energy* **2016**, *19*, 279–288.
- [24] S. J. R. Prabakar, J. Jeong, M. Pyo, *Electrochim. Acta* **2015**, *161*, 23–31.
- [25] W. Cai, Y.-X. Yao, G.-L. Zhu, C. Yan, L.-L. Jiang, C. He, J.-Q. Huang, Q. Zhang, *Chem. Soc. Rev.* **2020**, *49*, 3806–3833.
- [26] J. Zhang, W. Lv, D. Q. Zheng, Q. H. Liang, D. W. Wang, F. Y. Kang, Q. H. Yang, *Adv. Energy Mater.* **2018**, *8*, 1702395.

Manuscript received: December 2, 2020

Revised manuscript received: December 22, 2020

Accepted manuscript online: December 22, 2020

Version of record online: January 18, 2021